ALGORITHM THEORETICAL BASIS DOCUMENT

GOME-2 Sun-Induced Fluorescence of Terrestrial Ecosystems Retrieval

- SIFTER (v2.0) -

Prepared by:
Maurits KOOREMAN
Piet STAMMES
Olaf TUINDER
Folkert BOERSMA
Erik VAN SCHAIK
Santiago BOTIA

BETA VERSION

July 12, 2018

Royal Netherlands
Meteorological Institute
*Ministry of Infrastructure and the
Environment*

EUMETSAT
AC SAF
ATMOSPHERIC COMPOSITION
MONITORING

Contents

1 Introduction

1.1 Relevance

Human activities have dramatically influenced the global carbon cycle since the industrial revolution in the second half of the 18th century. The global average concentration of atmospheric carbon dioxide (CO_2) reached 390.5 ppm in 2011 and exceeded the 400 ppm level since; 40% higher than in 1750 [*Hartmann et al.*, 2013]. Higher atmospheric CO_2 concentrations and the associated increase of global mean surface temperatures are expected to affect many aspects of the terrestrial system, possibly for centuries to come [*Solomon et al.*, 2009].

Emitted CO_2 is not permanently stored in the atmosphere. Marine and terrestrial sinks remove approximately 55% of the emitted CO_2 (e.g. *Le Quéré et al.* [2015]). The main player in this process is the terrestrial biosphere, which assimilates atmospheric CO_2 during photosynthesis. The amount of carbon assimilation, or gross primary productivity (GPP), is the most uncertain flux within the global carbon budget [*Ciais et al.*, 2013]. By means of autotrophic respiration, vegetation also puts carbon back into the atmosphere resulting in a Net Ecosystem Exchange (NEE), which can be measured locally (e.g. by eddy-covariance flux towers). Computation of global gross carbon fluxes relies on input from a flux tower network, but there are only few such towers, especially in highly productive regions like the tropics. Necessary interpolation of the tower measurements results in uncertainties for global GPP estimates, currently estimated to be 123 ± 8 PgC yr^{-1} [*Beer et al.*, 2010]. The uncertainty is significant considering that we eventually want to estimate NEE and need to take into account errors in the respiratory processes as well. Recently, GPP was estimated from long-term atmospheric carbonyl sulfide (COS) observational records, suggesting substantial growth of GPP in the 20th century [*Campbell et al.*, 2017].

In addition to COS, remotely sensed vegetation fluorescence is a promising new global proxy for GPP. During photosynthesis, sunlight is absorbed by chlorophyll pigments in leaves and converted into chemical energy. Approximately 80% of the harvested energy is used for photosynthesis. Most of the rest is dissipated non-radiatively as heat and a small fraction ($\sim$1%) is emitted at longer wavelengths as fluorescence. This Sun-Induced Fluorescence (SIF) has a spectrally smooth signature with peaks at 690 (red fluorescence) and 737 nm (far-red fluorescence). Chlorophyll itself re-absorbs fluorescence within the canopy at wavelengths below 700 nm. Hence, the far-red SIF emission peak is more suitable for satellite observations.

Other measures of vegetation like the Normalized Difference Vegetation Index (NDVI) use the greenness of leaves as indicator of chlorophyll content. Unfortunately, chlorophyll content adapts slowly to stress (it can take weeks for leaves to lose their green color) and is therefore not as useful as a proxy for direct GPP. As photosynthesis is the core mechanism that drives both carbon assimilation and fluorescence, fluorescence can be exploited to serve as a more direct proxy for GPP. Previous studies have shown that fluorescence and GPP correlate linearly at leaf level, even under drought conditions [*Flexas et al.*, 2002, *Schreiber and Bilger*, 1987].

1.2 Measuring Fluorescence from Space

Top of atmosphere radiance measurements contain contributions of many components.
Space based spectrometers observing this spectral region with sufficient spectral resolution and signal to noise ratio are able to detect the SIF signatures in top-of-atmosphere (TOA) reflectance spectra. Following recent advancements in space borne observatories, methods have been developed to disentangle the small SIF signal from earthshine spectra. Initially, the retrieval
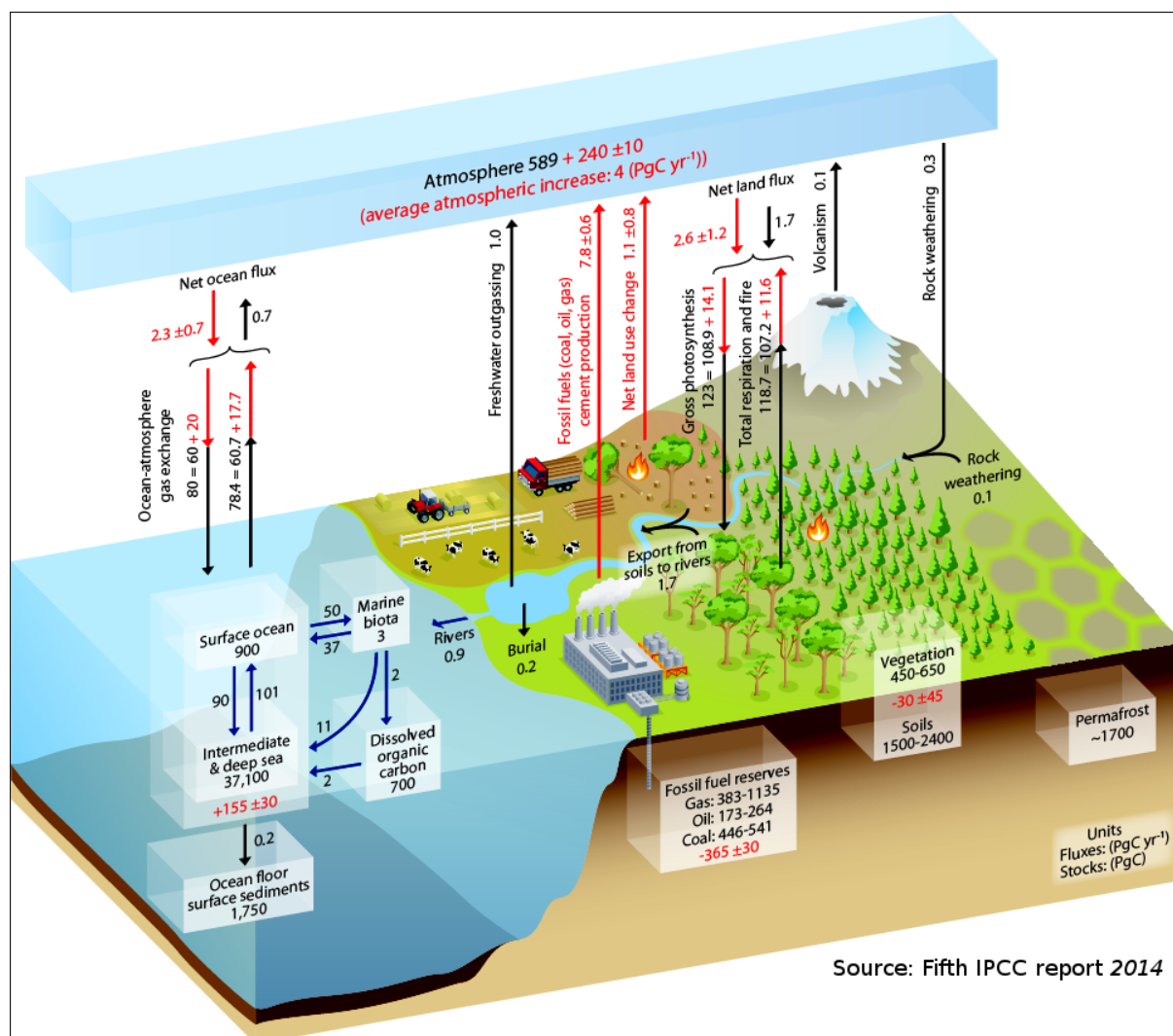
Figure 1: Illustration from the fifth IPCC report (2014) showing the different global carbon budgets. With 123 PgC yr^{-1}. Gross photosynthesis is one of the major atmospheric carbon sinks.

method relied on measuring the filling-in of solar Fraunhofer lines. This method requires a very high spectral resolution (typically < 0.05 nm) in order to resolve the individual Fraunhofer line structure and has been applied to space based instruments like the Greenhouse gasses Observing SATtelite (GOSAT) [*Frankenberg et al.*, 2011, *Joiner et al.*, 2012, 2011] and the Orbiting Carbon Observatory 2 (OCO-2) [*Frankenberg et al.*, 2014]. However, it comes at the cost of sparse spatial sampling. To obtain accurate information on global and seasonal SIF, better spatial and temporal coverage is needed. This is achieved for instance by the SCanning Imaging Absorption spectroMeter for Atmospheric CHartography (SCIAMACHY) [*Joiner et al.*, 2013, *Khosravi et al.*, 2015] and the Global Ozone Monitoring Instrument 2 (GOME-2) [*Joiner et al.*, 2013, *Köhler et al.*, 2015, *Sanders et al.*, 2016]. Future instruments capable of retrieving SIF include the TROPOspheric Monitoring Instrument (TROPOMI) [*Guanter et al.*, 2015] and the dedicated FLuorescence EXplorer (FLEX) [*Kraft et al.*, 2012].
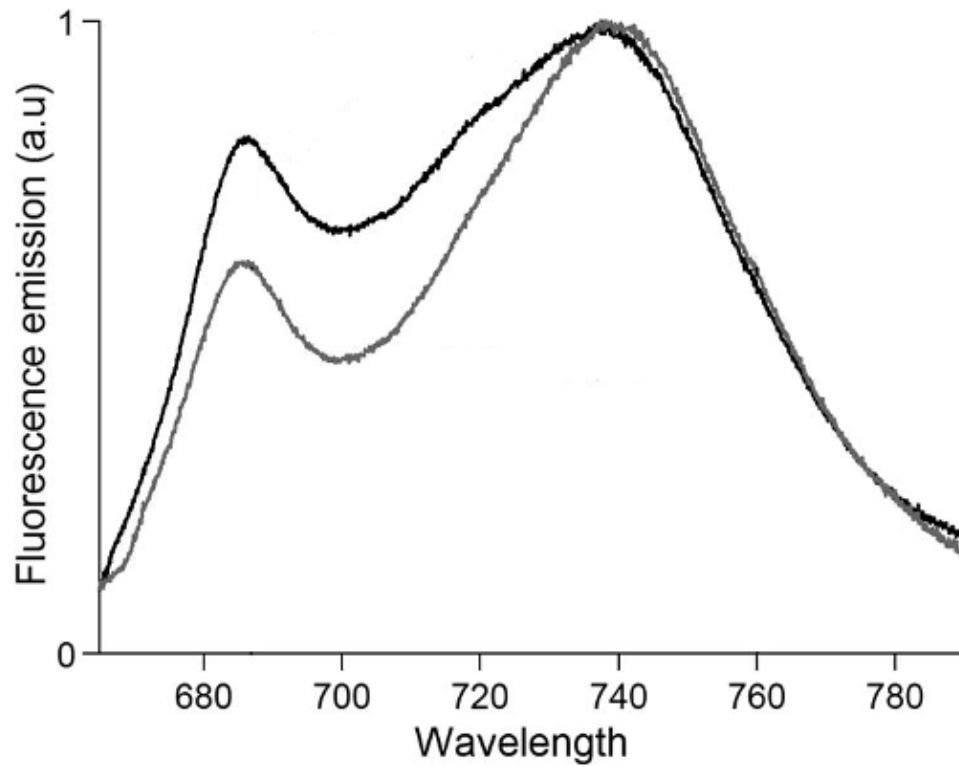
Figure 2: Chlorophyll fluorescence emission spectra at top of canopy for dense (grey) and sparse (black) leaf coverage. The discrepancy towards shorter wavelengths is caused by re-absorption of fluorescence by chlorophyll itself. Adopted from *Daumard et al.* [2012]
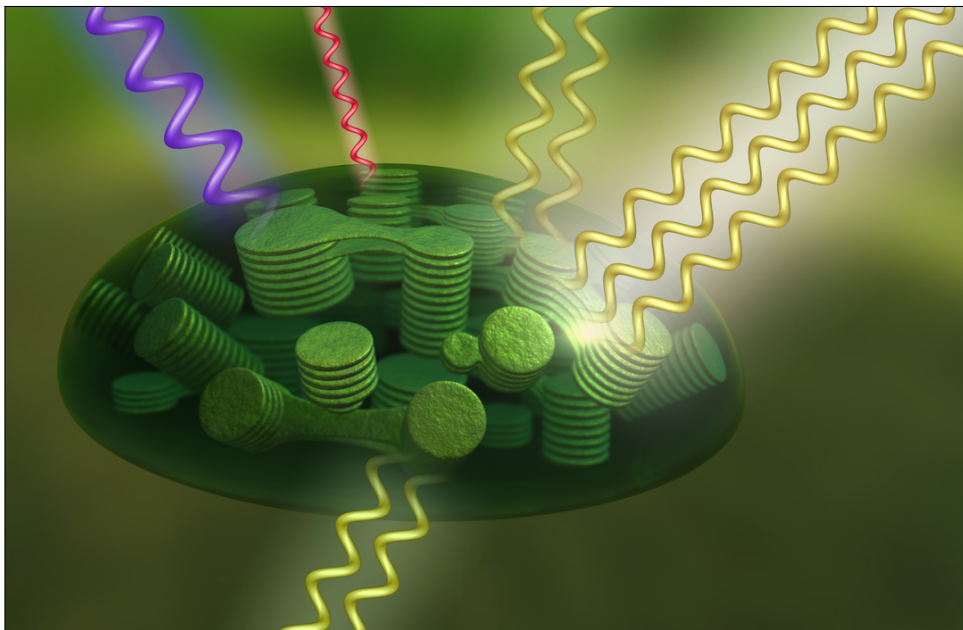

Figure 3: Schematic of chloroplast, the core of the photosynthetic mechanism. Approximately 80% of the harvested energy (bright minus dark yellow) is used for photosynthesis. $\sim$19% is dissipated non-radiatively as heat (purple) and a small fraction of $\sim$1% is emitted at longer wavelengths as fluorescence (red). Source: NASA

1.3   A new satellite product

The third Continuous Development and Operations phase (CDOP-3) of the Atmospheric Composition Satellite Application Facility (AC-SAF) started in March 2017 and will continue until February 2022. Within this framework a GOME-2 SIF product will be operationalized to fulfill user requirements and aid atmospheric trace gas retrieval.

2   Heritage

This paragraph is adopted from the Sanders et al. [2016] acknowledgements and author contributions sections.

In 2014, A.F.J. Sanders and W.W. Verstraeten initiated the research at KNMI. They supported and contributed to the development of the fluorescence processing code using GOME-2A data; they both developed analysis methods, assisted in the data interpretation, prepared figures/tables and authored *Sanders et al.* [2016]. Their work was co-funded by the Netherlands Organization for Scientific Research, NWO Vidi grant 864.09.001.

Sanders and Verstraeten also hosted internships for students from Utrecht University to work on the topic. In that framework, T.C. van Leth established the basic version of the processing code for retrieving fluorescence from GOME-2A, With the help and under supervision of Sanders and Verstraeten, he conducted preliminary sensitivity experiments and a preliminary SIF evaluation with GPP data. M.L. Kooreman revised and extended the basic processing code in order to process multiple years of data. Under supervision of Sanders and Verstraeten, he conducted a preliminary SIF evaluation with GPP data and assisted in the sensitivity experiments published in *Sanders et al.* [2016]. At this stadium, the published version of the fluorescence retrieval is called SIFTER, version 1 (SIFTERv1).

After Sanders and Verstraeten both left the KNMI, the development of the algorithm was continued by M. L. Kooreman and K. F. Boersma. Two additional students have since then worked to improve the SIFTERv1 algorithm, E. van Schaik and S. Botia.

Van Schaik used radiative transfer modeling to perform closed loop test and assess the algorithm robustness. His results are presented in chapter **??**. Based on this assessment, some modifications have been made to the algorithm, leading to SIFTERv2.

Botia has performed additional studies of the SIFTERv2 algorithm, primarily focusing on the reference set. Results of this study are presented in **??**
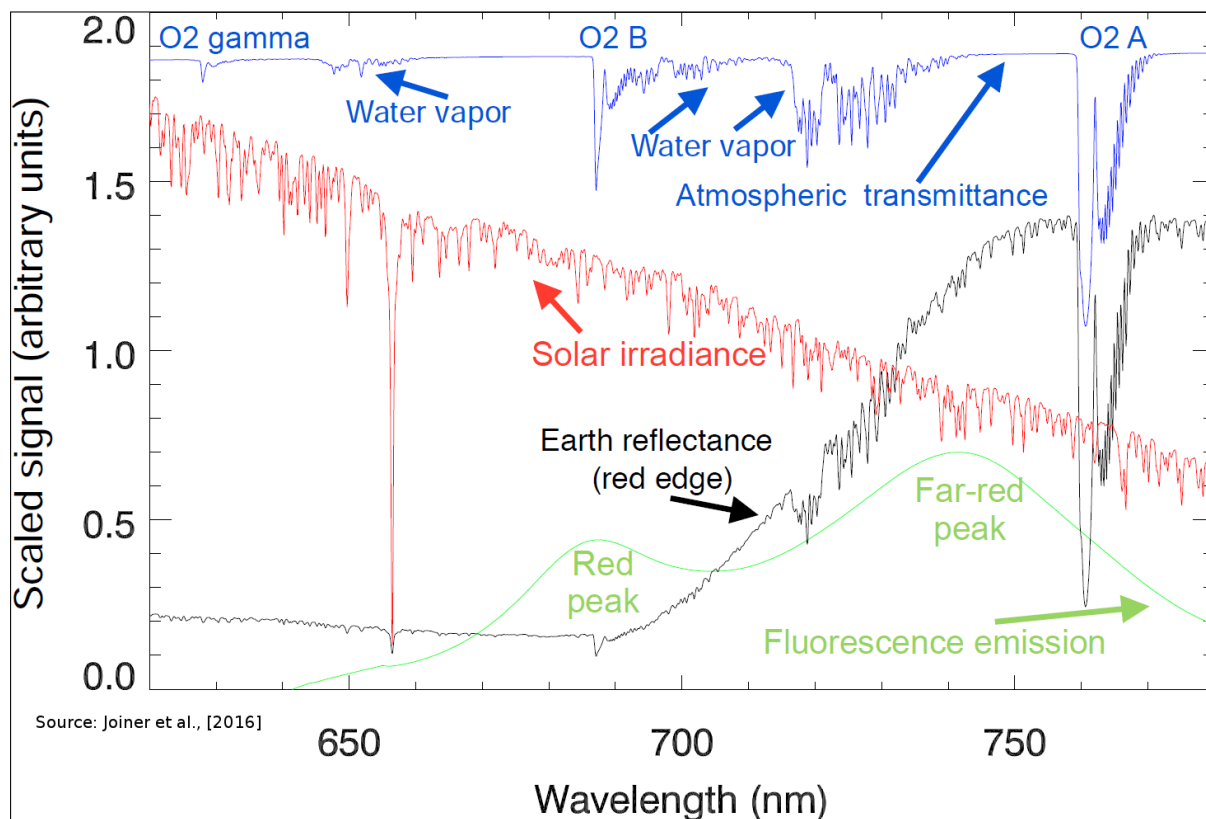
3   Retrieval algorithm description

Figure 4: On its way through the atmosphere, the solar irradiance spectrum (red) is altered by several components before it is detected by GOME-2. Most importantly the surface albedo (black) and the atmospheric transmittance (blue). Chlorophyll fluorescence (green) is added to the signal over vegetated areas. This figure is adopted from *Joiner et al.* [2016].

3.1   Methodology

The SIF retrieval is based on a data-driven (statistical) algorithm, developed by *Joiner et al.* [2013]. In this algorithm a forward model is constructed explaining the top-of-atmosphere reflectance spectrum in the near-infrared (NIR) region (in clear-sky situations) as a superposition of three terms: (1) an isotropic reflecting ground surface, (2) an isotropic fluorescence emission term, and (3) atmospheric transmittance (from e.g. water vapor), Fraunhofer lines and unresolved instrumental signatures (e.g. stray light). Rayleigh scattering is assumed to be negligible in the NIR wavelength region (see also *Frankenberg et al.* [2012]) and the monochromatic reflectance (R) can be written as

$$R(\lambda; \mu, \mu_0) \approx A_s(\lambda) T^\uparrow(\lambda; \mu) T^\downarrow(\lambda; \mu_0) + \frac{\pi I_F(\lambda) T^\uparrow(\lambda; \mu)}{\mu_0 E_0(\lambda)} \tag{1}$$

with μ and μ_0 the cosines of the viewing and solar zenith angles; I_F is the fluorescence emission, A_s is the surface albedo and E_0 is the solar irradiance at the top of atmosphere. $T^\uparrow$ and $T^\downarrow$ are the upward and downward atmospheric transmission factors, including only atmospheric extinction (no diffuse transmission). Any strong spectral variation of the top of atmosphere

reflectance is due to these quantities as well as Fraunhofer lines in the E_0 term. The surface albedo and fluorescence emission are assumed to be spectrally smooth.

To describe the atmospheric effects by a single parameter, the transmission terms are rewritten in terms of two-way slant absorption optical thickness through

$$T^\uparrow T^\downarrow = T^{\uparrow\downarrow} = e^{-\tau_s^{\uparrow\downarrow}} \tag{2}$$

where

$$\tau_s^{\uparrow\downarrow}(\lambda; \mu, \mu_0) = \tau_v\left(\frac{1}{\mu} + \frac{1}{\mu_0}\right) \tag{3}$$

and τ_v the vertical optical thickness.

We now have an expression for the two-way transmission applied to the surface albedo component of equation 1. The upwelling component $T^\uparrow$ applied to the fluorescence emission must also be written in terms of two-way slant optical thickness. To do so, $\tau^\uparrow$ has to be written in terms of $\tau^{\uparrow\downarrow}$

$$\tau_s^\uparrow(\lambda; \mu) = \tau_v\frac{1}{\mu} \cdot \overbrace{\left(\frac{\frac{1}{\mu} + \frac{1}{\mu_0}}{\frac{1}{\mu} + \frac{1}{\mu_0}}\right)}^{= 1} = \tau_s^{\uparrow\downarrow}\frac{\frac{1}{\mu}}{\frac{1}{\mu} + \frac{1}{\mu_0}}. \tag{4}$$

Equation 1 can now be rewritten as

$$R(\lambda; \mu, \mu_0) \approx A_s(\lambda)e^{-\tau_s^{\uparrow\downarrow}(\lambda)} + \frac{\pi I_\mathrm{F}(\lambda)e^{-\frac{\mu^{-1}}{\mu^{-1}+\mu_0^{-1}}\tau_s^{\uparrow\downarrow}(\lambda)}}{\mu_0 E_0(\lambda)}. \tag{5}$$

In the retrieval, equation 5 is applied to the spectral window between 734 nm to 758 nm. This includes some water vapor absorption up to about 740 nm but excludes the strong O_2-A absorption band at 760 nm.

4   Sensitivity analysis

In order to assess algorithm robustness, a study was conducted using synthetic top of atmosphere spectra. The benefit of using modeled spectra is the ability to control all parameters. The study uses the radiative transfer model Determining Instrument Specifications and Analyzing Methods for Atmospheric Retrieval (DISAMAR). This model can compute top-of-atmosphere reflectance spectra with a superimposed fluorescence signal. This allows for end-to-end tests of the SIFTER algorithm.

For a detailed description of these analysis we refer to *van Schaik et al., 2018*.

5 Application to GOME-2 measurements

5.1 GOME-2 Instrument

The GOME-2 spectrometers aboard the MetOp satellite series fly in a sun-synchronous polar orbit with a local equator crossing time of 9:30 a.m. on the descending node. For this retrieval, band 4 is used which has a spectral sampling rate of $\sim$0.2 nm and a spectral resolution of $\sim$0.5 nm. The scanning mirror of GOME-2 covers a 1920 km swath back (1.5 sec) and forth (4.5 sec) in 6 seconds. The integration time of the CCD-detector is 0.1875 seconds resulting in 24 forward pixels with a spatial resolution of 80-by-40 km and 8 backward pixels at 240-by-40 km. The GOME-2 instrument achieves global coverage in roughly 25 hours.

The relatively low spectral resolution of GOME-2 results in Fraunhofer line interference with atmospheric absorption lines within a single spectral bin. Therefore, method was developed by *Joiner et al.* [2013] which assumes the TOA radiance near 760 nm to be a superposition of three radiative components; surface reflectance, atmospheric absorption and SIF and calculates this absorption using a statistical method.

5.2 Level-1b pixel selection

The fluorescence retrieval requires only a selection of GOME-2 level-1 data. To limit data size, retrieval-specific level1b data are prepared. This selection is limited to band 4 (NIR) earth shine spectra. The large GOME-2 footprints often represent a mixture of different surface types (e.g. shrub land and rivers) which is undesirable for the retrieval. Because of their large footprint, backward scans are not used in the retrieval.

Pixels with the following specifics are rejected:

- Non Earth radiance measurements.

- Not in nadir observation mode.

- Integration time is not 0.1875 seconds

- Backward scans

- Within sun glint cone over sea ($\leq 18°$ scattering angle[1] over water)

Additionally, external cloud data from the GOME-2 FRESCOv7 database are collocated pixel by pixel and added to the dedicated level-1b extraction files. Collocation occurs by time stamp which provides a unique identifier for every GOME-2 pixel.

---

[1]The scattering angle is defined as: $\cos(\Theta) = \cos(\theta)\cos(\theta_0) + \sin(\theta)\sin(\theta_0)\cos(\phi - \phi_0)$

6   Level-1b to Level-2 processor: SIFTER

6.1   Forward model - application to spectrometer data

The extracted level-1b data are now ready to be processed to level-2 SIF data. In this section, the different components of the forward model are individually explained when they are applied to spectrometer data.

Reflectance measurement $R(\lambda)$
The monochromatic reflectance $R(\lambda)$ is replaced by the measured GOME-2 reflectance $R(\lambda_i)$, defined as the ratio between (terrestrial) radiance and (solar) irradiance.

Solar irradiance $E_0(\lambda)$
The monochromatic solar irradiance $E_0(\lambda)$ is replaced by the high-resolution solar irradiance reference spectrum from *Chance and Kurucz* [2010], convolved with the GOME-2 instrument response function $F_R(\lambda_i)$ and scaled to the actual sun-earth distance, denoted as $\hat{E}_0(\lambda_i)$. The scaling component is based on an elliptical orbit with an eccentricity e of 0.0167 and is calculated for each day of year d. The values 365, 89 and 3 correspond to the number of days in a year, the day of reference intensity of the high-resolution spectrum (March 29, 1992) and the approximate day of perihelion (January 3) respectively. Hence,

$$\hat{E}_0(\lambda_i) \approx (E_0(\lambda) * F_R(\lambda_i)) \cdot \frac{(1+e)\cos(\frac{2\pi}{365}(d-3))}{[(1+e)\cos(\frac{2\pi}{365}(d-89))]^2}. \tag{6}$$

Fluorescence emission I_F
The upwelling fluorescence radiance is parameterized as Gaussian curve with its peak located at (λ_F) 737.0 nm and a sigma-width (σ_F) of 33.9 nm following *Zarco-Tejada et al.* [2000]. Hence,

$$I_F(\lambda_i) \approx I_{F_0} e^{-\frac{1}{2}\left(\frac{\lambda_i - \lambda_F}{\sigma_F}\right)^2}, \tag{7}$$

where I_{F_0} is the fluorescence strength at 737 nm in Watts per square meter per steradian per nanometer (W m^{-2} sr^{-1} nm^{-1}).

Surface albedo A_s
The surface albedo is calculated by fitting a low-order polynomial function to the top of atmosphere reflectance spectral micro-windows where the atmospheric absorption is close to zero (i.e. where all light comes from the surface): 712 - 713 nm, 748 - 757 nm and 775 - 785 nm.

$$A_s \approx \sum_{j=0}^{n} a_j \lambda_i^j \tag{8}$$

In the actual retrieval, n=4. This order is required to model the spectral variability of vegetated surfaces known as the red-edge (see e.g. *Tilstra et al.* [2017]).

Two-way slant absorption optical thickness $\tau_s^{\uparrow\downarrow}$
GOME-2 spectra are selected over the Sahara region between latitudes 16N and 30N and longitudes 8W and 29E (see Fig. 5 and included in a reference set only if they are absolutely free of vegetation according to the 1 km resolution USGS Global Land Cover Characterization database (version 2; https://lta.cr.usgs.gov/GLCC) and if the scene effective cloud fraction in
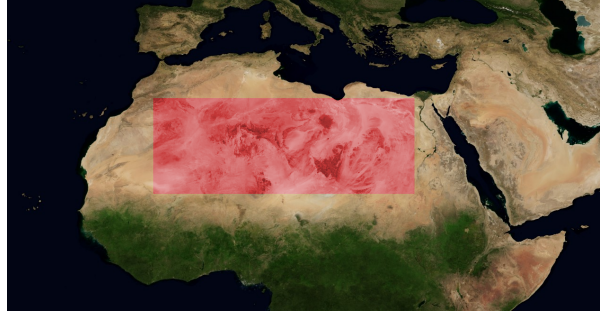
Figure 5: Measurements over a section (red) of the Sahara desert are used to build a reference atmospheric slant optical thickness.

the infra-red is below 0.4. The cloud fraction is taken from the GOME-2 FRESCO cloud retrieval [*Koelemeijer et al.*, 2001, *Wang et al.*, 2008, 2010].

The two-way slant absorption optical thickness is determined in a statistical way. The Sahara reference scenes contain no vegetation and thus, $I_F=0$. The last term in equation 5 cancels and two-way slant optical thickness $\tau_s^{\uparrow\downarrow}$ can be written as

$$\tau_s^{\uparrow\downarrow}(\lambda) \approx -\ln\left(\frac{R_{\text{ref}}(\lambda; \mu, \mu_0)}{A_s(\lambda)}\right),$$ (9)

where R_{ref} is the reflectance of the reference scene. Next, a number of sub-windows is selected for which the absorption optical thickness becomes very small (i.e. all radiation comes from the surface) to determine the surface albedo. Selected sub-windows are 712-713 nm, 748-757 nm and 775-783 nm. A second order polynomial (equation 8; $n=4$) is fitted to the measured reflectance in these windows to calculate $A_s(\lambda)$.

On an aggregate of reflectances from all scenes that match above criteria, principal component (PC) analysis is performed using the non-linear iterative partial least squares (NIPALS) algorithm [*Wold*, 1966, 1973] to determine the Empirical Orthogonal Functions (EOFs) $f_k(\lambda)$. Only the first 10 principal components are used as this is the optimal number to describe the atmospheric two-way slant absorption optical thickness without fitting noise. It is assumed that this set of basis EOFs can be used to describe the atmospheric two-way slant absorption optical thickness over all target scenes, including scenes with vegetation as

$$\tau_s^{\uparrow\downarrow}(\lambda_i) \approx \sum_{k=0}^{m} b_k f_k(\lambda_i)$$ (10)

Where b_k is the principal component associated with each EOF (f_k).

The forward model for the fluorescence retrieval is now completed and written as

$$R(\lambda; \mu, \mu_0) \approx \left(\sum_{j=0}^{n} a_j \lambda_i^j\right) e^{-\sum_{k=0}^{m} b_k f_k(\lambda_i)} + \frac{\pi I_{F_0} e^{-\frac{1}{2}\left(\frac{\lambda_i - \mu_F}{\sigma_F}\right)^2}}{\mu_0 \hat{E}_0(\lambda)} e^{-\frac{\mu^{-1}}{\mu^{-1} + \mu_0^{-1}} \sum_{k=0}^{m} b_k f_k(\lambda_i)}.$$ (11)

The retrieval operates by applying a Levenberg-Marquardt least-squares regression to minimize the differences between the observed and modeled reflectance for every pixel. It does so by optimizing for the 1+5+10=16 ($I_{F_0} + a_j + b_k$) free fitting parameters for every ground pixel.

6.2   Retrieval settings summary

Table 1: Parameter settings for SIFTER.

Parameter	Values/Range
Level-1b selection	
Measurement type	Radiance
Observation mode	Nadir
Integration time	0.1875 s
Scan mode	Forward
Sunglint cone (over water)	SCA $\leq 18°$
Calculating $\tau_s^{\uparrow\downarrow}(\lambda)$	
Reference set period	23-Jan-2007 until 31-Dec-2012
Spectral windows with no absorption	712-713 nm, 748-757 nm, 775-785 nm
Surface polynomial order	2nd
Number of principal components	10
NIPALS convergence target	10^{-8}
Upper cloud fraction	0.4
Retrieval settings	
Spectral fit window	734-758 nm
Surface polynomial order	4th
Peak of SIF curve	737.0 nm
Sigma width of SIF curve	33.7 nm
Upper cloud fraction	0.4
Post processing settings	
Mean residual (RMS) upper limit	0.01
Residual autocorrelation upper limit	0.2
Solar Zenith Angle upper limit	70°
Grid size	0.5°
Algorithm version	**2.0**

7   Level-2 to Level-3 post processing

The Level-3 processor takes the individual pixels and averages daily and monthly measurements on a 0.5x0.5 degree global grid. During this step a few post processing steps are taken to reduce noise and correct for biases.

7.1   Latitude bias correction

Although some red fluorescence by phytoplankton can penetrate through the water and reach the TOA, the far-red fluorescence is assumed to be invisible from space. The ocean is therefore an excellent region to use as zero reference for offset correction. Figure 6 shows that a latitudinal dependency is visible in the data with slightly negative values in the north and positive values in the south. We hypothesize that this is due to a small instrument temperature change during the sunlit side overpass.
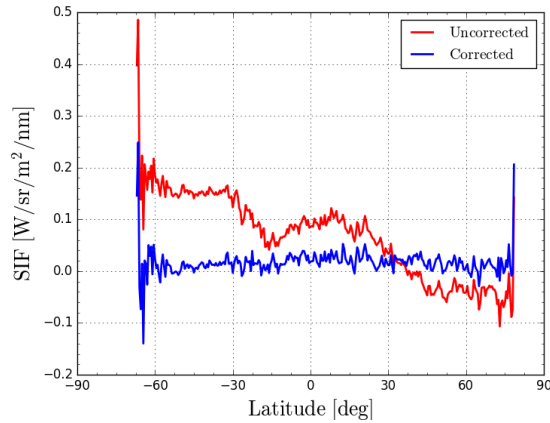

Figure 6: Latitudinal cross-section of zonal mean SIF over the ocean uncorrected (red) and corrected (blue).

To correct this a sample of ocean pixels is taken every day for all latitudes within a band of 5 latitudinal degrees. Pixels are only selected if they are completely surrounded by ocean pixels, to avoid accidentally including vegetation pixels. If there is at least 10 valid pixels within the latitude band, a linear regression is performed by determining the relation between the radiance and the SIF

$$R = a \cdot F_s + b \tag{12}$$

This yields a slope (a) and intercept (b) which are used to correct all pixels on that latitude. In essence, each retrieval is corrected based on the relationship between the radiance and the retrieved SIF value.

7.2   Noise correction

In order to reduce noise two additional post-processing filters are applied. Primarily a fit residual threshold is installed to reject pixels with a wavelength average RMS residual of 0.01. After this, the autocorrelation of each fit residual is calculated by

$$R(\tau) = \frac{\sum [X_\tau - \mu)(X_{\tau+1} - \mu)]}{\sigma^2}. \tag{13}$$
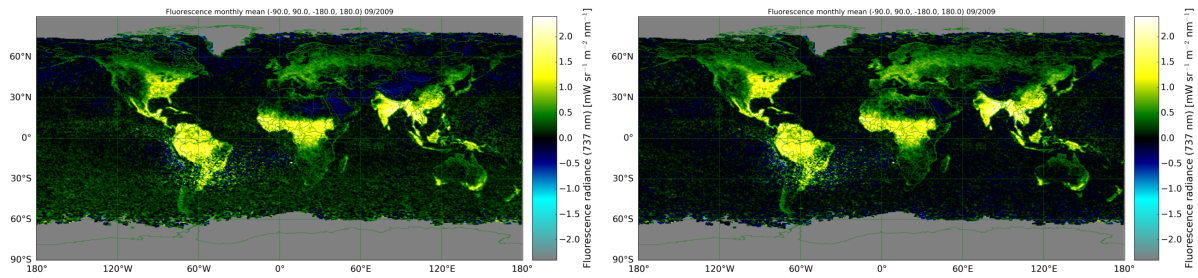
Figure 7: SIF retrieval uncorrected for high radiance scenes (left) and corrected (right). Especially over the ocean a latitudinal smoothing is visible, but also across Russia SIF values are clearly higher. Moreover, negative values over bright scenes such as the Sahara and the Taklamakan Desert are largely compensated.

Where X_τ is the spectral residual and $X_{\tau+1}$ is the spectral residual shifted one wavelength bin. μ and σ^2 are the mean and variance of the residual.

It is then assumed that random noise does not autocorrelate and pixels that show a wavelength averaged autocorrelation of over 0.2 are filtered out from the results. Figure 8 shows the spatial distribution of the rejected pixels. The South Atlantic Anomaly is strongly represented. Tropical forests also contribute partly to this noise, as well as some individual orbits, as seen over the Sahara. The filter reduces the amount of pixels by approximately 10%; a reasonable cost to gain ratio.
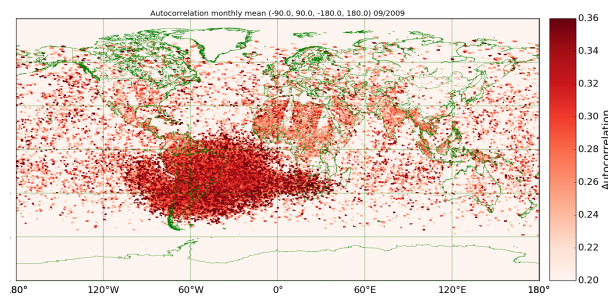

Figure 8: Global map of monthly mean autocorrelation (Sep-2009). Fit residues show the highest autocorrelation in the South Atlantic Anomaly region.

8   Results

A sample of level-3 data is shown in Figure **??**. Monthly mean SIF data is plotted on a 0.5-by-0.5 degree grid. The spatial structures of the SIF signal closely resemble vegetation. Moreover the global seasonal cycle of vegetation can clearly be seen moving north and south throughout the year.

9   References

Beer, C., et al., Terrestrial Gross Carbon Dioxide Uptake: Global Distribution and Covariation with Climate, *Science*, *329*, 834, doi:10.1126/science.1184984, 2010.

Campbell, J. E., J. A. Berry, U. Seibt, S. J. Smith, S. A. Montzka, T. Launois, S. Belviso, L. Bopp, and M. Laine, Large historical growth in global terrestrial gross primary production, *Nature*, *544*, 84–87, doi:10.1038/nature22030, 2017.

Chance, K., and R. L. Kurucz, An improved high-resolution solar reference spectrum for earth's atmosphere measurements in the ultraviolet visible, and near infrared, *Journal of Quantitative Spectroscopy & Radiative Transfer*, *111*, 1289–1295, doi:10.1016/j.jqrst.2010.01.036, 2010.

Ciais, P., et al., *Carbon and Other Biochemical Cycles. In: Climate Change 2013: The Physical Science Basis. Contribution of Working Group I to the Fifth Assessment Report of the Intergovernmental Panel on Climate Change*, Cambridge University Press, Cambridge, UK and New York, NY, USA, 2013.

Daumard, F., Y. Goulas, S. Champagne, F. A., A. Ounis, A. Olioso, and I. Moya, Continuous monitoring of canopy level sun-induced chlorophyll fluorescence during the growth of a sorghum field, *IEEE Trans. Geoscience and Remote Sensing*, *50*, 4292–4300, 2012.

Flexas, J., J. Mariano Escolona, S. Evain, J. Gulías, I. Moya, C. B. Osmond, and H. Medrano, Steady-state chlorophyll fluorescence (Fs) measurements as a tool to follow variations of net CO_2 assimilation and stomatal conductance during water-stress in C_3 plants, *Physiologia Plantarum*, *114*, 231–240, 2002.

Frankenberg, C., C. O'Dell, L. Guanter, and J. McDuffie, Remote sensing of near-infrared chlorophyll fluorescence from space in scattering atmospheres: implications for its retrieval and interferences with atmospheric CO_2 retrievals, *Atmospheric Measurement Techniques*, *5*, 2081–2094, doi:10.5194/amt-5-2081-2012, 2012.

Frankenberg, C., C. O'Dell, J. Berry, L. Guanter, J. Joiner, P. Köhler, R. Pollock, and T. E. Taylor, Prospects for chlorophyll fluorescence remote sensing from the Orbiting Carbon Observatory-2, *Remote Sensing of Environment*, *147*, 1–12, doi:10.1016/j.rse.2014.02.007, 2014.

Frankenberg, C., et al., New global observations of the terrestrial carbon cycle from gosat: Patterns of plant fluorescence with gross primary productivity, *Geophysical Research Letters*, *38*, L17,706, 2011.

Guanter, L., et al., Potential of the TROPOspheric Monitoring Instrument (TROPOMI) onboard the Sentinel-5 Precursor for the monitoring of terrestrial chlorophyll fluorescence, *Atmospheric Measurement Techniques*, *8*, 1337–1352, doi:10.5194/amt-8-1337-2015, 2015.

Hartmann, D. L., et al., Observations: Atmosphere and Surface, *Climate Change 2013: The Physical Science Basis. Contribution of Working Group I to the Fifth Assessment Report of the Intergovernmental Panel on Climate Change*, pp. 159–251, 2013.

Joiner, J., Y. Yoshida, A. P. Vasilkov, E. M. Middleton, P. K. E. Campbell, Y. Yoshida, A. Kuze, and L. A. Corp, Filling-in of near-infrared solar lines by terrestrial fluorescence and other geophysical effects: simulations and space-based observations from SCIAMACHY and GOSAT, *Atmospheric Measurement Techniques*, *5*, 809–829, doi:10.5194/amt-5-809-2012, 2012.

Joiner, J., L. Guanter, R. Lindstrot, M. Voigt, A. P. Vasilkov, E. M. Middleton, K. F. Huemmrich, Y. Yoshida, and C. Frankenberg, Global monitoring of terrestrial chlorophyll fluorescence from moderate-spectral-resolution near-infrared satellite measurements: methodology, simulations, an application to GOME-2, *Atmos. Meas. Tech.*, *6*, 2803–2823, 2013.

Joiner, J., Y. Yoshida, L. Guanter, and E. M. Middleton, New methods for the retrieval of chlorophyll red fluorescence from hyperspectral satellite instruments: simulations and application to gome-2 and sciamachy, *Atmos. Meas. Tech.*, *9*, 3939–3967, 2016.

Joiner, J., et al., First observations of global and seasonal terrestrial chlorophyll fluorescence from space, *Biogeosciences*, *8*, 637–651, doi:10.5194/bg-8-637-2011, 2011.

Khosravi, N., M. Vountas, V. V. Rozanov, A. Bracher, A. Wolanin, and J. P. Burrows, Retrieval of Terrestrial Plant Fluorescence Based on the In-Filling of Far-Red Fraunhofer Lines Using SCIAMACHY Observations, *Frontiers in Environmental Science*, *3, 78*, doi:10.3389/fenvs.2015.00078, 2015.

Koelemeijer, R. B. A., P. Stammes, J. W. Hovenier, and J. F. de Haan, A fast method for retrieval of cloud parameters using oxygen A band measurements from the Global Ozone Monitoring Experiment, *Journal of Geophysical Research*, *106*, 3475–3490, 2001.

Köhler, P., L. Guanter, and J. Joiner, A linear method for the retrieval of sun-induced chlorophyll fluorescence from GOME-2 and SCIAMACHY data, *Atmospheric Measurement Techniques*, *8*, 2589–2608, doi:10.5194/amt-8-2589-2015, 2015.

Kraft, S., U. Del Bello, M. Bouvet, M. Drusch, and J. Moreno, FLEX: ESA's Earth Explorer 8 candidate mission, *Proceedings of 2012 IEEE International Geoscience and Remote Sensing Symposium, Munich, Germany, 22-27 July.*, pp. 7125–7128, 2012.

Le Quéré, C., et al., Global Carbon Budget 2015, *Earth System Science Data*, *7*, 349–396, doi:10.5194/essd-7-349-2015, 2015.

Sanders, A. F. J., W. W. Verstraeten, M. L. Kooreman, T. C. van Leth, J. Beringer, and J. Joiner, Spaceborne Sun-Induced Fluorescence Time Series from 2007 to 2015 Evaluated with Australian Flux Tower Measurements, *Remote Sensing*, *8*, doi:10.3390/rs8110895, 2016.

Schreiber, U., and W. Bilger, *Rapid assessment of stress effects on plant leaves by chlorophyll fluorescence measurements.*, Plant Response to Stress, Edited by J. D. Tenhunen et al. Springer-Verlag, Heidelberg, Berlin, 1987.

Solomon, S., G.-K. Plattner, R. Knutti, and P. Friedlingstein, Irreversible climate change due to carbon dioxide emissions, *Proceedings of the Natural Acadamy of Sciences*, *106*, 1704–1709, doi:10.1073/pnas.0812721106, 2009.

Tilstra, L. G., O. N. E. Tuinder, P. Wang, and P. Stammes, Surface reflectivity climatologies from UV to NIR determined from Earth observations by GOME-2 and SCIAMACHY, *Journal of Geophysical Research: Atmospheres*, *122*, doi:10.1002/2016JD025940, 2017.

Wang, P., P. Stammes, R. van der A, G. Pinardi, and M. van Roozendael, FRESCO+: an improved O_2 a-band cloud retrieval algorithm for tropospheric trace gas retrievals, *Atmospheric Chemistry and Physics Discussions*, *3*, 2008.

Wang, P., O. Tuinder, and P. Stammes, Cloud retrieval algorithm for GOME-2: FRESCO+, *Tech. rep.*, Royal Dutch Meteorological Institute, 2010.

Wold, H., Estimation of Principal Components and related models by iterative least squares., *Multivariate Analysis*, 1966.

Wold, H., Nonlinear Iterative Partial Least Squares NIPALS modeling: Some current developments., *Multivariate Analysis*, 1973.

Zarco-Tejada, P. J., J. R. Miller, G. H. Mohammed, and T. L. Noland, Chlorophyll Fluorescence Effects on Vegetation Apparent Reflectance: I. Leaf-Level Measurements and Model Simulation, *Remote Sensing of Environment*, *74*, 582–595, 2000.